Manipulation of Exchange Bias Effect via All-Solid-State Li-Ion Redox Capacitor with Antiferromagnetic Electrode

Zeeshan Mustafa,[1,2,3,4] Dhanapal Pravarthana⊙,[1,2] Baomin Wang⊙,[1,2,*] Huali Yang,[1,2] and
Run-Wei Li[1,2,3,†]

[1]*CAS Key Laboratory of Magnetic Materials and Devices, Ningbo Institute of Materials Technology and Engineering, Chinese Academy of Sciences, Ningbo 315201, People's Republic of China*

[2]*Zhejiang Province Key Laboratory of Magnetic Materials and Application Technology, Ningbo Institute of Materials Technology and Engineering, Chinese Academy of Sciences, Ningbo 315201, People's Republic of China*

[3]*Center of Materials Science and Optoelectronics Engineering, University of Chinese Academy of Sciences, Beijing 100049, People's Republic of China*

[4]*Lahore Garrison university, Lahore 52400, Punjab, Pakistan*

The electric field control of the exchange bias has considerable application scope in modern spintronic devices such as magnetic random-access memories. Herein, we utilize an all-solid-state Li-ion redox capacitor with an antiferromagnetic electrode for reversible control of the exchange bias in a Co/Co_3O_4 heterostructure. The controlled intercalation and deintercalation of Li ions in the antiferromagnetic Co_3O_4 anode via galvanostatic charge and discharge enables reversible and nonvolatile control of the exchange bias. The mechanism of exchange-bias control in the Co/Co_3O_4 heterostructure is studied using various characterization techniques. This work establishes an approach to control the exchange bias in all-solid-state magnetoionics, which is of great practical importance for the development of modern spintronic devices.

I. INTRODUCTION

Exchange bias (EB) is the phenomenon of pinning of magnetic spins at the interface of a ferromagnetic (FM) material and an antiferromagnetic (AF) material. This is due to the exchange coupling of spins at the FM-AF interface leading to a shift in the magnetic hysteresis loop. The EB phenomenon plays an important role in the development of modern spintronic devices such as magnetic read head and magnetic random-access memory; the pinned FM layer in these devices acts as a reference layer [1–3]. For the past few years, electric-field-controlled EB has gained considerable attention because it facilitates the development of low-power-consuming tunable EB systems [4]. The FM layer of an EB system can be tuned by interfacing it with a piezoelectric material so that the strain in the piezoelectric material is transferred to the FM thin film, thereby altering the EB field (H_{EB}) value [5–8]. The EB effect can also be controlled by the modulation of the charge carrier density at the surface of a metallic AF material, wherein the applied voltage leads to an exertion of force on the exchange spring that results in a positive or

negative shift in H_{EB}, depending on the sign of the voltage bias [9]. EB control has recently been realized by an electric-current-induced spin-orbit torque that leads to a positive or negative horizontal EB shift in the hysteresis loop at low temperatures, depending on the polarity of the current pulse [10].

Utilization of electrically driven ion migration for tuning the magnetic properties of materials shows surprising results [11–18]. Achieving ionics-controlled magnetism via oxygen ion migration has shown great potential in modulating the properties of magnetic materials; in this case the electric-field-control coefficient $\beta > 5000$ f J $(V m)^{-1}$, is much larger than that achieved by previously employed electric-field-controlled methods. The electric-field-control coefficient β is defined as the change in interfacial magnetocrystallline anisotropy energy per voltage per length units [15,19]. In particular, the ionics-controlled approach can be used for reversible toggling of the state from AF to FM via O^{2-} migration in $SrCoO_{2.5}$ at low voltages [11]. The EB effect can also be tuned by electrically driven O^{2-} migration in $Pt/Co/Ni/HfO_2$ [20] and $Si/SiO_2/Pt/Co/NiO/Pt$ [21]. Li-ion migration is more efficient in controlling the magnetic properties as it facilitates better diffusion at room temperature owing to its rich chemistry [12]. Li-ion migration promotes the

*wangbaomin@nimte.ac.cn
†runweili@nimte.ac.cn

control of remnant magnetization of bulk magnetic material, magnetic cycling, on-off magnetism, and magnetic anisotropy [22–25]. Herein, we utilize the all-solid-state Li-ion redox capacitor to control the EB of the Co/Co_3O_4 heterostructure by electric-field-induced Li-ion migration. Li-ion transport into the AF Co_3O_4 electrode leads to a redox process via a conversion reaction between oxygen ions that produces a spin disorder in the AF. The mechanism of Li-ion-migration-controlled EB is studied by using various characterization techniques. This study provides an approach to control the EB in all-solid-state magnetoionics.

II. EXPERIMENT

A. Sample preparation

For fabrication of the proposed all-solid-state Li-ion redox capacitor, Li-ion conducting glass ceramic (LICGC) (general composition: Li_2O-Al_2O_3-SiO_2-P_2O_5-GeO_2) sheets are used as the solid electrolyte as well as the substrate. A 250-nm-thick film of $LiCoO_2$ is deposited on one side of the polished LICGC as the cathode material for Li-ion supply via pulsed laser deposition (PLD). The substrate temperature is maintained at 600 °C under 20 Pa oxygen pressure. In order to obtain a Pt electrode that acts as a current colectore, a 70-nm-thick Pt layer is deposited over $LiCoO_2$ substrate via dc magnetron sputtering at 0.6-Pa Ar pressure and 20-W power. Before depositing Co_3O_4 films, the other side of the LICGC is polished using a diamond-polishing liquid to remove the silver paste that is used as a glue to clamp the LICGC on the sample holder for $LiCoO_2$ growth. Co_3O_4 films of 30–60 nm thicknesses are deposited via PLD at a deposition temperature of 600 °C under 30 Pa oxygen pressure. A Co film of thickness 20 nm is deposited over Co_3O_4 via dc magnetron sputtering at 1.2-Pa Ar pressure and 20-W power, as the substrate temperature is maintained at 120 °C. Subsequently, over the Co thin film, the Pt electrode is deposited as the current collector.

B. Structural and magnetic characterization

XRD is carried out using the Bruker D8 DISCOVER diffractometer (Cu K_α, $\lambda = 1.5406$ Å) to characterize the crystal phases of the deposited thin films of Co, Co_3O_4 and $LiCoO_2$ at a scan rate of 0.02° s^{-1}. Magnetic hysteresis (*MH*) loop measurements are performed using a superconducting quantum interference device (SQUID). The Bruker Dimension Icon atomic force microscopy (AFM) integrated with conductive atomic force microscopy (cAFM) facilitated the visualization of the nanoscale lithiation process of Co_3O_4. The Kratos AXIS Ultra DLD x-ray photoelectron spectroscopy (XPS) facilitated the investigation of the pristine and lithiated states of the Co_3O_4 film prepared

by etching the upper two thin films of Pt and Co. The etching process is carried out by Ar-ion milling using a beam energy of 4 kV, an extract current of 100 μA, and a raster size of 3 mm. *In situ* Raman spectroscopy is performed to investigate the change in the stretching and bending modes of the charged and discharged states using the Renishaw Invia Reflex Raman spectrometer. The Auriga Carl Zeiss dual beam-focused ion beam is used to prepare the sample for HRTEM. HRTEM is performed using a Talos F200x, Themo Fisher microscope at an operating voltage of 200 kV to investigate the device structure.

C. Electrochemical characterization

A Zahner Zennium electrochemical workstation is used to measure cyclic voltammetry (CV) and galvanostatic charge-discharge (GCD) cycles in the all-solid-state Li-ion redox capacitor. The CV measurements are performed at a potential difference of −1 to 2.5 V at a scan rate of 100 mV s^{-1}. The GCD is performed at a range of 5–15 μA cm^{-2} current densities in the potential difference of 0 to 1.75 V. Across all the measurements, Co_3O_4 is used as the working electrode, while $LiCoO_2$ acts as the reference and counter electrodes.

III. RESULTS AND ANALYSIS

A. EB effect of the Co/Co_3O_4 heterostructure

The XRD spectra of the as-deposited films of $Pt/Co/Co_3O_4/LICGC$, shown in Fig. 1(a), confirm a crystalline structure of the deposited thin films. The indexed peaks at 38.27°, 44.4°, and 40° correspond to the (*hkl*) planes of $Co_3O_4(222)$, Co(111), and Pt(111), respectively [26]. All other peaks correspond to the reflections of the LICGC solid electrolyte. The average values of roughness of the Co_3O_4 and Co thin films are 2 and 1.3 nm, respectively, as obtained from the topographic images as shown in Figs. 1(b) and 1(c), respectively. To investigate EB in the Co/Co_3O_4 heterostructure, we fix the Co layer thickness to 20 nm and vary the thickness of Co_3O_4 from 30 to 60 nm. The observed normalized *MH* loops for the Co/Co_3O_4 heterostructure with 50-nm Co_3O_4 at different temperatures are shown in Fig. 1(d). The high onset temperature of 150 K observed in the fresh sample can be attributed to the formation of a thin layer of CoO at the Co/Co_3O_4 interface [27]. Further, high H_{EB} of 980 Oe at 10 K is observed; this is much larger than the previously reported H_{EB} values [27,28]. The interfacial roughness of FM and AF and the thickness of the AF layer play important roles in the development of a thin-film-based EB system [29,30]. The combined effect of the optimal roughness of FM and AF films at their interface can lead to a large EB resulting from the presence of uncompensated spins [31–34]. The effect of the thickness of Co_3O_4 on H_{EB} is shown in Fig. 1(e). An increase in H_{EB} is observed with
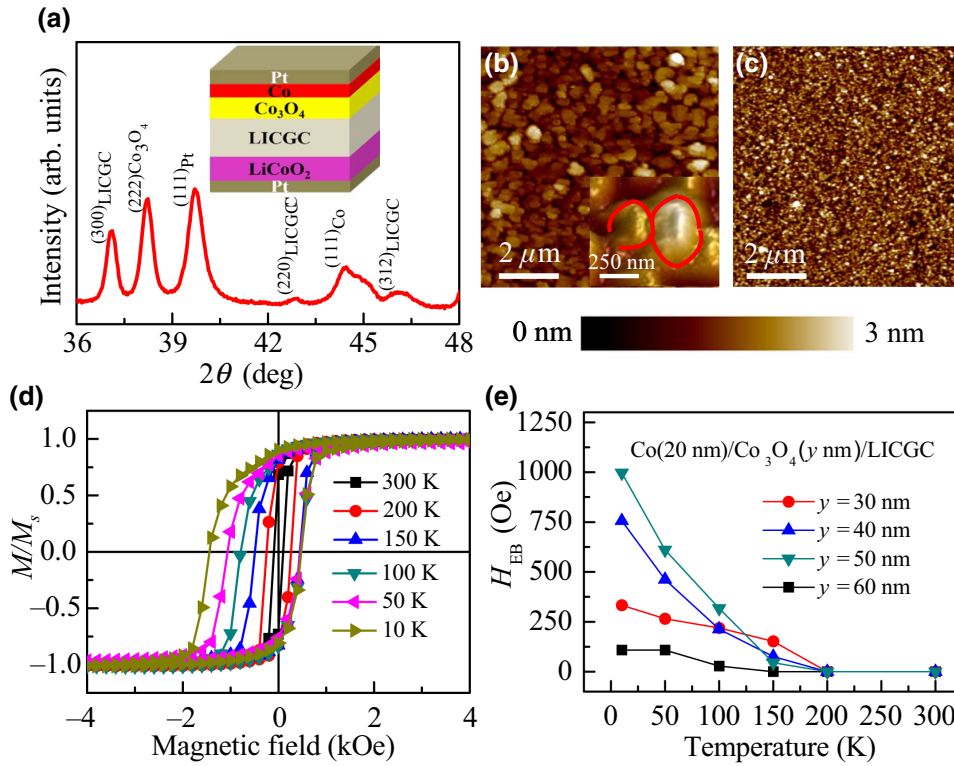
FIG. 1. (a) XRD spectra of as-deposited Co/Co$_3$O$_4$ bilayer. Inset shows the schematic of all-solid-state Li-ion redox capacitor. (b) Topographic image obtained using the AFM tapping mode for Co$_3$O$_4$. The inset shows magnified topographic image with grain boundaries highlighted with red line. (c) Topographic image of Co films deposited on LICGC. (d) Normalized *MH* loop measured at different temperatures for Co(20 nm)/Co$_3$O$_4$(50 nm) bilayer deposited on LICGC. (e) H_{EB} versus temperature for Co(20 nm)/Co$_3$O$_4$ bilayer with Co$_3$O$_4$ thickness ranging from 30 to 60 nm.

an increase in the thickness of Co$_3$O$_4$ up to 50 nm; a further increase in the thickness of Co$_3$O$_4$ decreases H_{EB}. This thickness dependence of H_{EB} can be understood better from the EB domain-state model that predicts the formation of more domain-state spins on increasing the thickness of AF; it also predicts the defect in AF that causes high H_{EB} [35]. It also shows an increase in H_{EB} as the temperature decreases, and a prominent effect is observed at 10 K below the Néel temperature of Co$_3$O$_4$. Thus, the high H_{EB} can be attributed to the optimal roughness and thickness of the AF Co$_3$O$_4$ layer.

B. Control of EB by Li-ion transport

Figure 2(a) shows the CV curves of the Pt/Co/Co$_3$O$_4$/ LICGC/LCO/Pt structure. The bias voltage is applied to the top and bottom Pt electrodes of the two-electrode system as shown in Fig. 2(a). The peak at 1.45 V corresponds to the oxidative peak, and two prominent reductive peaks are observed at the potential differences of 0.08 V and −0.5 V; this is consistent with the previous report on the Li-ion intercalation and deintercalation in Co$_3$O$_4$ [36]. The oxidative and reductive peaks govern the reversible electrochemical reaction that takes place between an electropositive Li ion and an electronegative oxygen ion via conversion reactions. It should be noted experimentally that no redox reactions or Li ions can be stored in the Co film due to their inability to react with Li ions. This also proves that oxidation and redox reactions occur in Co$_3$O$_4$

only during Li-ion intercalation and deintercalation at different electrode potentials [37]. The GCD is performed for the all-solid-state capacitor in a potential difference of 0–1.75 V at current densities of 5, 10, and 15 μA cm^{-2}, as shown in Fig. 2(b). It is observed that specific capacity is high in the case of 5 μA cm^{-2}. The device shows good GCD stability for 500 cycles at a current density of 5 μA cm^{-2} [Fig. 2(c)]. After the first charge and discharge, only 2% irreversible capacity loss is observed, and it is stable up to 500 charge-discharge cycles. This confirms that the material is highly stable. In the charge-discharge profile, a nonlinear behavior is observed; this confirms an electrochemical redox reaction that occurs during the Li-ion intercalation and deintercalation. Quantification of the number of Li ions (x) per formula unit of Co$_3$O$_4$ can be determined under constant current electrolysis using Faraday's laws of electrolysis given by

$$x = \frac{C M_{\mathrm{wt}}}{F}$$

where M_{wt} is the molecular weight of Co$_3$O$_4$, F is the Faraday constant, and C is the specific charge capacity. The value of x depends on the GCD potential difference but not linearly even in the constant current density [Fig. 2(c)].

In the pristine state, the observed normalized *MH* loop at 10 K exhibits H_{EB} of 980 Oe. The EB decreases as the potential difference reaches a critical value. This happens because for a small value of applied potential difference the number of Li-ion concentration is very minimal. When
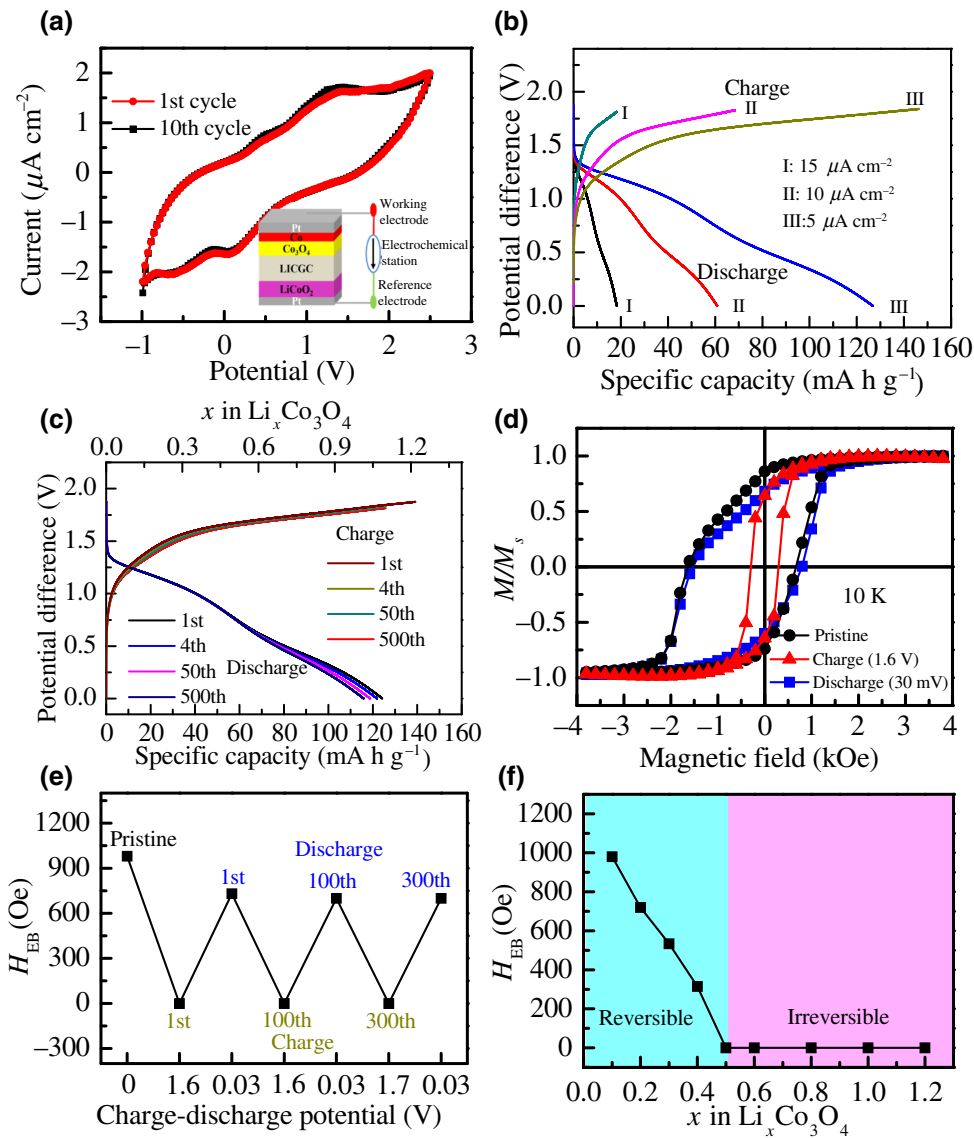
FIG. 2. (a) Cyclic voltammograms performed on Co_3O_4 as working electrode in the all-solid-state Li-ion redox capacitor. The inset shows a schematic of GCD when potential difference is applied. (b) GCD at different current densities. (c) Voltage versus specific capacity/x in $Li_xCo_3O_4$ for current density $5\,\mu A\,cm^{-2}$ in different cycles. (d) Normalized *MH* loop measured at 10 K using SQUID VSM at pristine, charged, and discharged states. (e) Modulation of H_{EB} as a function of galvanostatic charge-discharge voltage from pristine state. (f) H_{EB} versus different values of x in $Li_xCo_3O_4$.

crossing a critical value, the increase of the potential difference increases Li-ion content in the Co_3O_4 electrode. After the first charge with $x = 0.5$, the observed normalized *MH* loop shows no EB due to distortion at the interface [Fig. 2(d)]. As the sample is discharged in a potential difference of 0.03 V, H_{EB} returns to 731 Oe; while discharging, EB is observed below 40 K, so the onset temperature changes permanently with respect to the original state. This can be attributed to the irreversible distortion in the CoO layer because no EB is observed at 150, 100, and 50 K. Thus, the EB onset temperature observed at 10 K after the first discharge confirms that the Co layer is

exchange coupled with Co_3O_4. This decrease in H_{EB} can be attributed to irreversible capacity loss that leads to irreversible structural changes. After the first charge-discharge process, the reversible control of EB is observed up to the 100th and 300th GCD cycles [Fig. 2(e)]. Further, H_{EB} is measured as a function of x in $Li_xCo_3O_4$, where x is in the range of 0.2 to 1.2, as shown in Fig. 2(f). H_{EB} gradually decreases as x increases from 0.2 to 0.5. There is no EB as x ranges from 0.5 to 1.2. It is observed that for $x \leq 0.5$, the control of EB is reversible, but for $x \geq 0.5$, the control of EB is irreversible. Since the GCD is reversible for $x \geq 0.5$, so the irreversibility in the EB can be attributed to
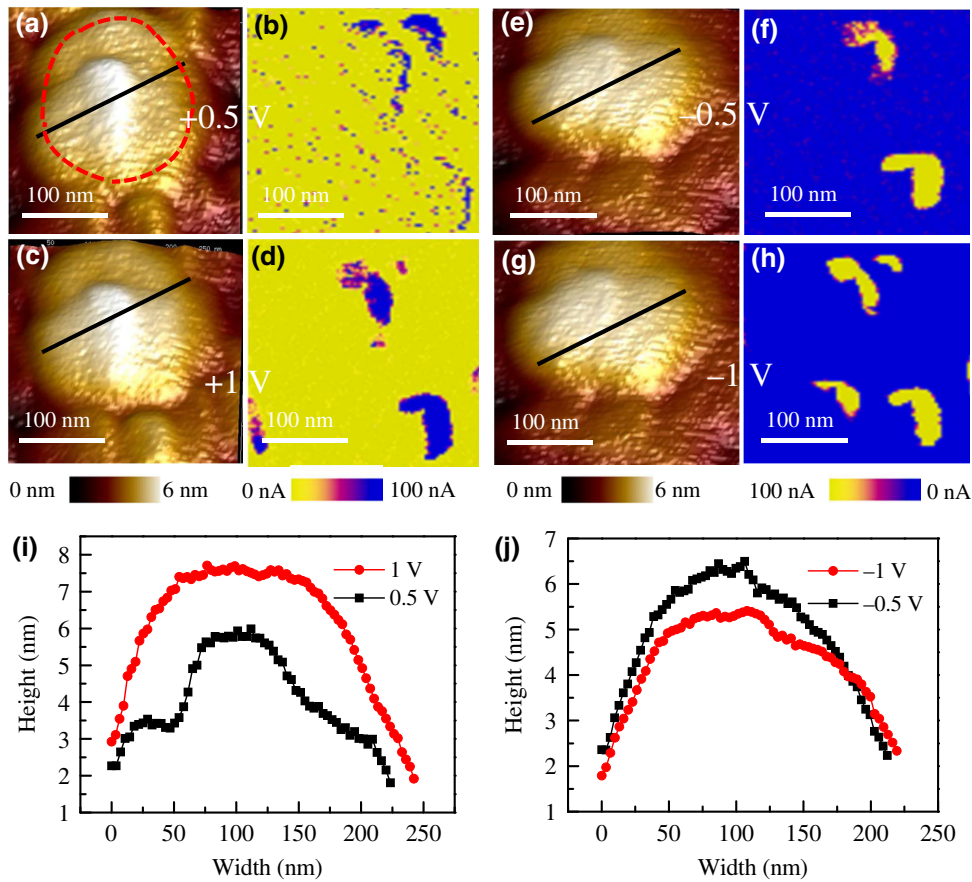
FIG. 3. Topographic and TUNA current images for (a), (b) 0.5 V, (c), (d) 1 V, (e), (f) −0.5 V, and (g), (h) −1 V. The dotted red line in Fig. 3(a) indicates the grain boundary. Typical topography line-scan profiles for (i) positive and (j) negative bias voltage.

a permanent change in magnetic ordering of the Co/Co$_3$O$_4$ heterostructure. It is important to understand the mechanism of EB control by Li-ion intercalation and to determine the cause of irreversibility of EB for $x \geq 0.5$. The visualization of Li-ion transport into Co$_3$O$_4$ is imaged via cAFM to understand the process of Li-ion intercalation and deintercalation. Further, to determine the cause of irreversibility of EB for $x \geq 0.5$, the lithium-inserted samples with values of x equal to 0 (pristine state), 0.5, and 1.2 are investigated by advanced structural characterization techniques such as XPS, Raman spectroscopy, and TEM. These studies are detailed in the subsequent sections.

C. Direct observation of Li-ion transport into the Co$_3$O$_4$ film

The cAFM studies are performed under different voltage-bias magnitudes and polarities to directly observe the Li-ion intercalation and deintercalation in Co$_3$O$_4$ thin films without the deposition of Co/Pt layers on top, as shown in Fig. 3. The cAFM scan is performed on Co$_3$O$_4$ deposited over LICGC/LiCoO$_2$/Pt. The topographic and tunneling AFM (TUNA) current images are recorded under positive and negative sample bias voltages applied to the bottom Pt electrode. LiCoO$_2$ being positively biased with respect to the bottom Pt electrode, the Li ions are

forced toward Co$_3$O$_4$ as the negative charge stored in Co$_3$O$_4$ attracts the Li ions toward LiCoO$_2$. The topographic images at 0 V for large-scale dimensions, such as $6 \times 6 \ \mu m^2$ and $750 \times 750 \ nm^2$, are shown in Fig 1(b) and in the inset of Fig. 1(b), respectively. The typical topographic and TUNA current image for voltage biases of 0.5 and 1 V are shown in Figs. 3(a) and 3(c), respectively. The cAFM and TUNA current image in Fig. 3(b) shows the upward current flow in blue color at the junctions between the grains [Fig. 3(a)]; this indicates that Li-ion intercalation is initiated at the grain boundaries; further increase in the bias voltage to 1 V expands the blue area at the grain boundaries, and the blue color is also observed inside the grains [Fig. 3(d)]. While reversing the polarity to negative voltage biases of −0.5 and −1 V, the downward current flow, indicated by yellow, is observed; this indicates the deintercalation of stored Li ions from the Co$_3$O$_4$ film, under a positive bias voltage. Moreover, the current contrasts are seen in the same region under positive and negative bias voltages, thereby indicating the reversibility of Li-ion intercalation and deintercalation at the grain boundaries and inside the grains [38,39]. The observation of Li-ion intercalation and deintercalation at the grain boundaries can be attributed to the high diffusion coefficient at the grain boundaries rather than inside the grains because of the presence of more defects at the grain boundary. Further,
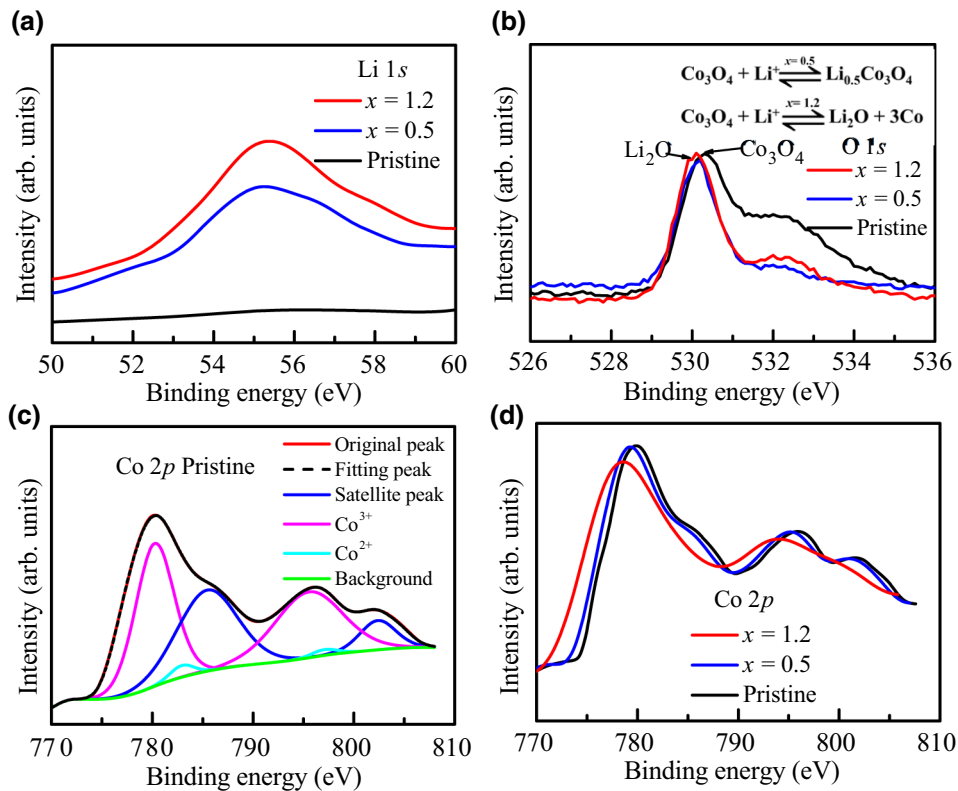
FIG. 4. XPS spectra of Co_3O_4 for (a) Li $1s$ and (b) O $1s$ for pristine, charged to $x = 0.5$ and $x = 1.2$. (c) Fitted XPS spectra of Co $2p$ for pristine state. (d) XPS spectra of Co $2p$ for pristine, charged to $x = 0.5$ and $x = 1.2$.

a slight change in topography indicates the possible volume expansion and contraction during Li intercalation and deintercalation. The region of volume expansion under positive bias over the region where lithium is inserted can be better seen from the line scan of the topographic image in Figs. 3(a) and 3(c). However, the volume expansion is shown in Fig. 3(i). The typical line-scan height increases under 1 V with respect to 0.5 V, which indicates the volume expansion locally due to lithium insertion, while under −1 V, the line-scan height decreases with respect to −0.5 V, which indicates the volume contraction due to Li deintercalation [Fig. 3(j)]. In this respect, XPS investigations are carried out to understand the electrochemical process in the lithium-inserted samples. To investigate the volume expansion during lithium insertion, Raman spectroscopy and TEM characterizations are performed to detail the bending and stretching vibration modes and lattice strain in the Co_3O_4 films, respectively.

D. Li-ion transport induced an electrochemical effect in the Co_3O_4 film

The XPS investigation is carried out on $Li_xCo_3O_4$ films with values of x equal to 0 (pristine state), 0.5, and 1.2 after removing the Pt and Co layers in the Li-ion redox capacitor by argon-ion etching in the XPS chamber. The XPS core spectra of Li $1s$, O $1s$, and Co $2p$ are shown in Fig. 4. The Li $1s$ spectra in the pristine state show no peaks, while in the charged samples with x equal to 0.5 and 1.2, the presence of Li $1s$ core XPS peak is observed at

55 eV [Fig. 4(a)]. Furthermore, the peak intensity increases for $x = 1.2$ due to an increase in the concentration of Li ions. The O $1s$ XPS spectra show a peak at 529.35 eV that corresponds to the cobalt oxide bond in the pristine state [Fig. 4(b)]. After charging to $x = 0.5$ (blue curve), the O $1s$ spectra show a little red shift, while for $x = 1.2$ (red curve) it undergoes a more prominent red shift owing to the formation of Li_2O via conversion reactions between Li ions and oxygen ions from Co_3O_4 [40]. The XPS spectra of Co $2p$ for the pristine state exhibit two prominent peaks at 781.61 and 797.66 eV, which correspond to Co $2p_{3/2}$ and Co $2p_{1/2}$, respectively, with satellite feature fitted with different components as shown in Fig. 4(c). The fitting of the Co $2p_{3/2}$ and Co $2p_{1/2}$ XPS spectra can be better understood from the spinel structure of Co_3O_4 that exhibits two oxidation states: Co^{2+} (tetrahedral coordination) and Co^{3+} (octahedral coordination). The components of Co^{2+} and Co^{3+} in the XPS spectra occur at the upper (magenta curve) and lower (cyan curve) binding energies for both Co $2p_{3/2}$ and Co $2p_{1/2}$ levels, respectively. In the charged Co_3O_4 films with values of x equal to 0.5 (blue curve) and 1.2 (red curve), a red shift in the Co $2p_{3/2}$ and Co $2p_{1/2}$ levels is observed [Fig. 4(d)] with respect to the Co $2p$ XPS spectra in the pristine state. For the sample charged to $x = 0.5$ (blue curve), a red shift is exhibited in the Co $2p_{3/2}$ and Co $2p_{1/2}$ XPS spectra. This confirms that the electrochemical redox process occurs when Li ions move into Co_3O_4. In Co_3O_4, the Co^{3+} (octahedral) oxidation state has 16 interstitial sites; this is more than the 8
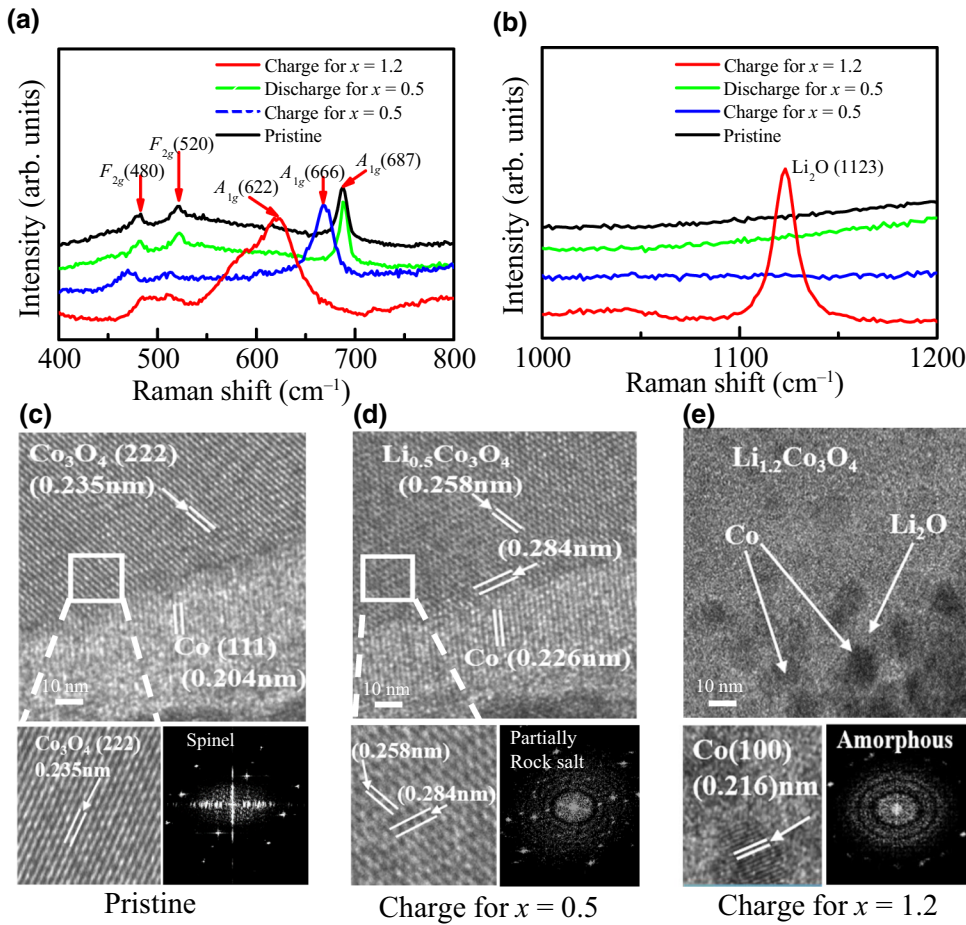
(a)

(b)

FIG. 5. Raman spectra for pristine, charged to $x = 0.5$ and $x = 1.2$ in the range of (a) 400 to 800 cm^{-1} and (b) 1000 to 1200 cm^{-1}. TEM images of Co/Co_3O_4 heterostructure in (c) pristine state, (d) charged to $x = 0.5$, and (e) charged to $x = 1.2$. In addition, the enlarged region of Co_3O_4 and its corresponding FFT are shown for (c), (d), and (e).

(c) Pristine

(d) Charge for $x = 0.5$

(e) Charge for $x = 1.2$

interstitial sites of the Co^{2+} (tetrahedral) oxidation state. Consequently, the inserted Li ions prefer the tetrahedral interstitial sites due to availability of large bonding vacancies wherein they bond with oxygen leading to a red shift. The sample charged to $x = 1.2$ (red curve) exhibits a large red shift, and the Co $2p_{3/2}$ peak occurs at 778.32 eV, which corresponds to the Co metallic state. This confirms that the lithiation process occurs via conversion reactions.

E. Li-ion-transport-induced strain in the Co_3O_4 film

In the pristine state, the Raman spectra show three active modes A_{1g} (687 cm^{-1}), F_{2g} (520 cm^{-1}), and F_{2g} (480 cm^{-1}) that correspond to the stretching and bending vibrations of the Co − O bond [Fig. 5(a)]; this agrees well with the previously reported literature of Co_3O_4 [41]. The F_{2g} mode corresponds to the combined vibrations of Co^{3+} and Co^{2+} at the octahedral and tetrahedral sites, respectively, while the A_{1g} mode corresponds to the stretching vibration of Co(III) oxide bond at the octahedral site. There is a reversible peak shift in the Raman spectra of the A_{1g} mode after the GCD for $x = 0.5$ during the 100th charge-discharge cycle. However, no peak shift is observed in the F_{2g} vibration mode. After Li-ion insertion, the large shift in the A_{1g} mode compared to the shift in the F_{2g} vibration

mode can be attributed to the preferential diffusion of the Li ions in the octahedral interstitial sites rather than the tetrahedral interstitial sites in the Co_3O_4 spinel structure, owing to the availability of more interstitial positions in the octahedral site in comparison to the tetrahedral site. Indeed, in a previous study, it was found that a single Li atom is energetically unstable in the tetrahedral site because the Fermi energy for a single Li atom in the tetrahedral site is 1.349 eV, whereas it is −1.544 eV in the octahedral site [42]. Thus, while charging Co_3O_4 with a Li-ion value of $x \leq 0.5$, the Li ions prefer to occupy the octahedral Co^{3+} sites, thereby straining the Co − O stretching band. After discharge, the Raman peak corresponding to the A_{1g} mode reverted to the original position. However, for $x = 1.2$, the shift in the A_{1g} mode is larger, as compared to $x = 0.5$ as shown in Fig. 4(a) [41]. In addition, the Raman peak at 1123 eV corresponds to Li_2O for $x = 1.2$, as shown in Fig. 4(b) [41]. Further, the Raman shift of the A_{1g} mode occurs toward the lower side (red shift) after lithiation that can lead to strain in the Co_3O_4 lattice [41]. To quantitatively understand this strain in the Co_3O_4 lattice after lithiation, TEM investigations are carried out on pristine and charged samples. Figure 5(c) shows the interface of the Co/Co_3O_4 lattice structure in the pristine state. The average values of d spacing measured via HRTEM
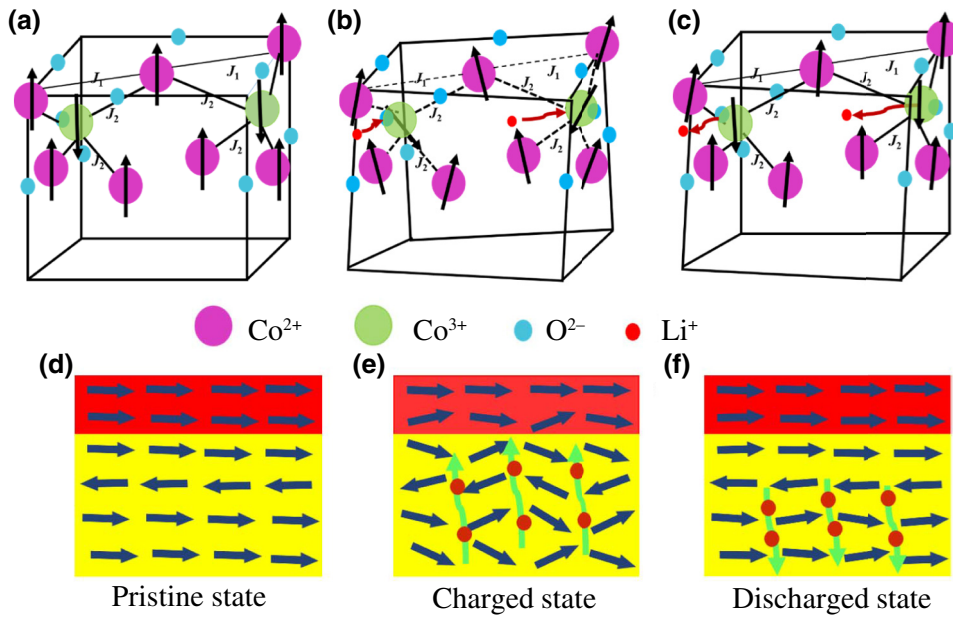
FIG. 6. Schematic of spin arrangement in Co_3O_4 unit cell for (a) pristine, (b) charged, and (c) discharged states. Schematic of manipulation of EB via Li-ion in (d) pristine, (e) charged, and (f) discharged states.

for Co and Co_3O_4 are 0.235 and 0.204 nm, respectively. The calculated d spacing from the HRTEM corresponds to the $Co_3O_4(222)$ and $Co(111)$ planes which agree well with the XRD spectra shown in Fig. 1(a). The magnified view of the Co_3O_4 HRTEM lattice structure confirms the ordered structure of Co_3O_4 in the pristine state. The corresponding fast Fourier transform (FFT) image confirms the spinel structure of Co_3O_4 [43,44]. After charging to $x = 0.5$, the d spacing in $Li_xCo_3O_4$ increases in the lithiated region to 0.258 and 0.284 nm [Fig. 5(d)]; this corresponds to a partial rock-salt crystal structure [44]. It also confirms the volume expansion in the lithiated region that was previously inferred from the cAFM study. When $x = 1.2$, the Co_3O_4 structure completely transforms into amorphous Li_2O and Co metal [Fig. 5(e)]. The halo-diffused FFT confirms the presence of amorphous Li_2O formation. This observation of Li_2O and Co metal formation is consistent with a previous study of XPS and Raman spectroscopy when $Li_xCo_3O_4$ is charged to $x = 1.2$.

IV. DISCUSSION

A schematic of the spin arrangements in Co_3O_4 unit cell for pristine, charged, and discharged states are shown in Figs. 6(a)–6(c), respectively. The schematic of the Co_3O_4 unit cell shows the atomic positions of Co^{3+} (octahedral) and Co^{2+} (tetrahedral) in green and purple colors, respectively. The superexchange interactions among Co^{2+} sublattices through FM coupling are denoted by J_1, while the superexchange interactions between Co^{2+} and Co^{3+} sublattices through AF coupling are denoted by J_2 [45]. J_2 is stronger than J_1 because of purely AF spin interactions resulting from the AF ordering below Néel temperature due to a fully paired electronic structure. In the pristine state, the FM spins in Co and the AF spins in Co_3O_4 are

coupled owing to the exchange interaction between the spins at the interface of Co and Co_3O_4 bilayers thereby exhibiting the EB effect as shown in Fig. 6(d). In the charged state, Li ion prefers the octahedral site to the tetrahedral site in the Co_3O_4 lattice, as indicated by red color in Fig. 6(d); this is in accordance with the results of Raman analysis. Further, Li-ion insertion into the Co_3O_4 lattice can induce strain effects, as detailed previously in Raman and TEM analyses, thereby confirming the strain and volume expansion in the Co_3O_4 unit cell. As a result, Li insertion can distort the AF coupling J_2 due to the strain effect, as shown in Fig. 6(b). Thus, the disorder in the AF Co_3O_4 induces disorder at the interface of the Co/Co_3O_4 heterostructure, as shown in Fig. 6(e), resulting in the reduction of H_{EB}, while in the discharge process, the spin order in Co_3O_4 is retained back to that of the pristine state. The schematic of Li-ion deinsertion is shown in Fig. 6(f). Thus, based on the XPS, Raman, and TEM analyses of $Li_xCo_3O_4$ for values of x equal to 0 (pristine state), 0.5, and 1.2, it is inferred that the reversibility of EB for $x \leq 0.5$ can be attributed to the reversible disorder in the Co_3O_4 structure. The reversible strain effect observed in the A_{1g} mode of the Raman spectra after GCD, as previously discussed, indicates the reversible switching of EB. However, for $x \geq 0.5$, the Co_3O_4 lattice structure completely transforms into amorphous Li_2O and Co metal formations thereby exhibiting irreversible switching of EB.

V. CONCLUSIONS

The Co/Co_3O_4 heterostructure exhibits EB with high H_{EB} of 980 Oe obtained for the all-solid-state Li-ion redox capacitor. The reversible and nonvolatile control of EB in the Co/Co_3O_4 heterostructure is achieved by inducing a reversible spin disorder in the AF Co_3O_4 via Li-ion

intercalation and deintercalation. The mechanism of EB control by Li intercalation and deintercalation is detailed by cAFM, XPS, Raman, and TEM characterizations. This study provides a method to modulate the properties of AF oxide materials in reversible and nonvolatile manners. In addition, based on lithium chemical reactions such as insertion, alloying, and conversion reactions, there are different ways to control the AF properties by using an all-solid-state Li-ion redox capacitor.

[1] R. Comstock, Review modern magnetic materials in data storage, J. Mater. Sci. Mater. **13**, 509 (2002).

[2] P. Grunberg, Exchange anisotropy, interlayer exchange coupling and GMR in research and application, Sensor Actuat. A-Phys. **91**, 153 (2001).

[3] M. Takagishi, K. Koi, M. Yoshikawa, T. Funayama, H. Iwasaki, and M. Sahashi, The applicability of CPP-GMR heads for magnetic recording, IEEE Trans. Magn. **38**, 2277 (2002).

[4] M. B. Jungfleisch, W. Zhang, and A. Hoffmann, Perspectives of antiferromagnetic spintronics, Phys. Lett. A **382**, 865 (2018).

[5] S. Polisetty, W. Echtenkamp, K. Jones, X. He, S. Sahoo, and C. Binek, Piezoelectric tuning of exchange bias in a BaTiO$_3$/Co/CoO heterostructure, Phys. Rev. B **82**, 134419 (2010).

[6] M. Liu, J. Lou, S. Li, and N. X. Sun, E-Field control of exchange bias and deterministic magnetization switching in AFM/FM/FE multiferroic heterostructures, Adv. Funct. Mater. **21**, 2593 (2011).

[7] S. Wu, J. Miao, X. Xu, W. Yan, R. Reeve, X. Zhang, and Y. Jiang, Strain mediated electric field control of exchange bias in a Co$_{90}$Fe$_{10}$/BiFeO$_3$/SrRuO$_3$/PMN-PT heterostructure, Sci. Rep. **5**, 8905 (2015).

[8] P. Li, C. Zhou, C. Cao, W. Wang, and C. Jiang, Electric field control of non-volatile 180° switching of the unidirectional anisotropy field in a multiferroic heterostructure, Phys. Chem. Chem. Phys. **20**, 25854 (2018).

[9] Y. Wang, X. Zhou, C. Song, Y. Yan, S. Zhou, G. Wang, C. Chen, F. Zeng, and F. Pan, Electrical control of the exchange spring in antiferromagnetic metals, Adv. Mater. **27**, 3196 (2015).

[10] P. H. Lin, B. Y. Yang, M. H. Tsai, P. C. Chen, K. F. Huang, H. H. Lin, and C. H. Lai, Manipulating exchange bias by spin–orbit torque, Nat. Mater. **18**, 335 (2019).

[11] N. Lu, *et al.*, Electric field control of tri-state phase transformation with a selective dual-ion switch, Nature **546**, 124 (2017).

[12] A. Molinari, H. Hahn, and R. Kruk, Voltage control of magnetism in all-solid-state and solid/liquid magnetoelectric composites, Adv. Mater. **31**, 1806662 (2019).

[13] U. Bauer, L. Yao, A. J. Tan, P. Agrawal, S. Emori, H. L. Tuller, S. Van Dijken, and G. S. Beach, Magneto-ionic control of interfacial magnetism, Nat. Mater. **14**, 174 (2015).

[14] C. Bi, Y. Liu, T. Newhouse-Illige, M. Xu, M. Rosales, J. Freeland, O. Mryasov, S. Zhang, S. Te Velthuis, and W. Wang, Reversible Control of Co Magnetism by Voltage-Induced Oxidation, Phys. Rev. Lett. **113**, 267202 (2014).

[15] B. Dieny and M. Chshiev, Perpendicular magnetic anisotropy at transition metal/oxide interfaces and applications, Rev. Mod. Phys. **89**, 025008 (2017).

[16] P. Dhanapal, T. Zhang, B. Wang, H. Yang, H. Xuan, C. Bi, W. Wang, and R.-W. Li, Reversibly controlled magnetic domains of Co film via electric field driven oxygen migration at nanoscale, Appl. Phys. Lett. **114**, 232401 (2019).

[17] R. Mishra, D. Kumar, and H. Yang, Oxygen Migration Based Spintronic Device Emulating a Biological Synapse, Phys. Rev. Appl. **11**, 054065 (2019).

[18] L. H. Diez, Y. Liu, D. Gilbert, M. Belmeguenai, J. Vogel, S. Pizzini, E. Martinez, A. Lamperti, J. Mohammedi, A. Laborieux, Y. Roussigne, A. J. Grutter, E. Arenholtz, P. Quarterman, B. Maranville, S. Ono, M. S. El Hadri, E. E. Fullerton, and L. S. Tejerina, A. Stashkevich, S.M. Cherif, A.D. Kent, D. Querlioz, J. Langer, B. Ocker, and D. Ravelosona, Nonvolatile Ionic Modification of the Dzyaloshinskii-Moriya Interaction, Phys. Rev. Appl. **12**, 034005 (2019).

[19] B. Cui, C. Song, F. Li, X. Zhong, Z. Wang, P. Werner, Y. Gu, H. Wu, M. Saleem, S. S. P. Parkin, and F. Pan, Electric Field Control of Oxygen Vacancies and Magnetic Phase Transition in a Cobaltite/Manganite Bilayer, Phys. Rev. Appl. **8**, 044007 (2017).

[20] X. Zhou, Y. Yan, M. Jiang, B. Cui, F. Pan, and C. Song, Role of oxygen ion migration in the electrical control of magnetism in Pt/Co/Ni/HfO$_2$ films, J. Phys. Chem. C **120**, 1633 (2016).

[21] L. Wei, Z. Hu, G. Du, Y. Yuan, J. Wang, H. Tu, B. You, S. Zhou, J. Qu, H. Liu, R. Zheng, Y. Hu, and J. Du, Full electric control of exchange bias at room temperature by resistive switching, Adv. Mater. **30**, 1801885 (2018).

[22] S. Dasgupta, B. Das, M. Knapp, R. A. Brand, H. Ehrenberg, R. Kruk, and H. Hahn, Intercalation-driven reversible control of magnetism in bulk ferromagnets, Adv. Mater. **26**, 4639 (2014).

[23] S. Dasgupta, B. Das, Q. Li, D. Wang, T. T. Baby, S. Indris, M. Knapp, H. Ehrenberg, K. Fink, R. Kruk, and H. Hahn, Toward on and off magnetism: Reversible electrochemistry to control magnetic phase transitions in spinel ferrites, Adv. Funct. Mater. **26**, 7507 (2016).

[24] X. Zhu, J. Zhou, L. Chen, S. Guo, G. Liu, R.-W. Li, and W. D. Lu, In situ nanoscale electric field control of magnetism by nanoionics, Adv. Mater. **28,** 7658 (2016).

[25] D. Pravarthana, B. Wang, Z. Mustafa, S. Agarwal, K. Pei, H. Yang, and R.-W. Li, Reversible Control of Magnetic Anisotropy and Magnetization in Amorphous $Co_{40}Fe_{40}B_{20}$ Thin Films via all-Solid-State Li-ion Redox Capacitor, Phys. Rev. Appl. **12,** 054065 (2019).

[26] D. De, O. Iglesias, S. Majumdar, and S. Giri, Probing core and shell contributions to exchange bias in Co/Co_3O_4 nanoparticles of controlled size, Phys. Rev. B **94,** 184410 (2016).

[27] B. You, Y. Wang, Y. Zhao, L. Sun, W. Sheng, M. Pan, J. Du, A. Hu, and M. Lu, Exchange bias in Co/Co_3O_4 bilayers, J. Appl. Phys. **93,** 6587 (2003).

[28] C. Vaz, E. Altman, and V. Henrich, Exchange bias and interface electronic structure in Ni/Co_3O_4 (011), Phys. Rev. B **81,** 104428 (2010).

[29] J. Nogues and I. K. Schuller, Exchange bias, J. Magn. Magn. Mater. **192,** 203 (1999).

[30] E. Demirci, M. Ozturk, R. Topkaya, S. Kazan, N. Akdogan, M. Obaida, and K. Westerholt, Thickness and temperature dependence of exchange bias in Co/CoO bilayers, J. Supercond. Nov. Magn. **25,** 2591 (2012).

[31] D. Lederman, J. Nogues, and I. K. Schuller, Exchange anisotropy and the antiferromagnetic surface order parameter, Phys. Rev. B **56,** 2332 (1997).

[32] J. Nogués, D. Lederman, T. Moran, I. K. Schuller, and K. Rao, Large exchange bias and its connection to interface structure in FeF_2–Fe bilayers, Appl. Phys. Lett. **68,** 3186 (1996).

[33] A. M. Choukh, Effect of interface on exchange coupling in NiFe/FeMn system, IEEE Trans. Magn. **33,** 3676 (1997).

[34] W. F. Egelhoff Jr, P. Chen, C. J. Powell, M. D. Stiles, and R. D. McMichael, Growth of giant magnetoresistance spin valves using indium as a surfactant, J. Appl. Phys. **79,** 2491 (1996).

[35] U. Nowak, K. D. Usadel, J. Keller, P. Miltényi, B. Beschoten, and G. Guntherodt, Domain state model for exchange bias. I. theory, Phys. Rev. B **66,** 014430 (2002).

[36] Z. W. Fu, Y. Wang, Y. Zhang, and Q. Z. Qin, Electrochemical reaction of nanocrystalline Co_3O_4 thin film with lithium, Solid State Ion. **170,** 105 (2004).

[37] V. Pralong, J. B. Leriche, B. Beaudoin, E. Naudin, M. Morcrette, and J. M. Tarascon, Electrochemical study of nanometer Co_3O_4, Co, $CoSb_3$ and Sb thin films toward lithium, Solid State Ion. **166,** 295 (2004).

[38] X. Zhu, C. S. Ong, X. Xu, B. Hu, J. Shang, H. Yang, S. Katlakunta, Y. Liu, X. Chen, L. Pan, J. Ding, and R.-W. Li, Direct observation of lithium-ion transport under an electrical field in Li_xCoO_2 nanograins, Sci. Rep. **3,** 1084 (2013).

[39] N. Balke, S. Jesse, Y. Kim, L. Adamczyk, A. Tselev, I. N. Ivanov, N. J. Dudney, and S. V. Kalinin, Real space mapping of Li-ion transport in amorphous Si anodes with nanometer resolution, Nano Lett. **10,** 3420 (2010).

[40] N. Mahmood, T. Tang, and Y. Hou, Nanostructured anode materials for lithium ion batteries: Progress, challenge and perspective, Adv. Energy Mater. **6,** 1600374 (2016).

[41] M. A. Islam, M. Zuba, V. DeBiase, N. Noviasky, and C. J. Hawley, High capacity lithium ion batteries composed of cobalt oxide nanoparticle anodes and Raman spectroscopic analysis of nanoparticle strain dynamics in batteries, Nanotechnology **29,** 075403 (2018).

[42] W. M. Lau and Y. Zhang, The electrochemical properties of Co_3O_4 as a lithium-ion battery electrode: A first-principles study, Phys. Chem. Chem. Phys. **20,** 25016 (2018).

[43] J. Li, K. He, Q. Meng, X. Li, Y. Zhu, S. Hwang, K. Sun, H. Gan, Y. Zhu, Y. Mo, E. A. Stach, and D. Su, Kinetic phase evolution of spinel cobalt oxide during lithiation, ACS Nano **10,** 9577 (2016).

[44] Q. Li, J. Wu, Z. Yao, Y. Xu, M. M. Thackeray, C. Wolverton, and V. P. Dravid, Dynamic imaging of metastable reaction pathways in lithiated cobalt oxide electrodes, Nano Energy **44,** 15 (2018).

[45] W. Roth, The magnetic structure of Co_3O_4, J. Phys. Chem. Solids **25,** 1 (1964).